JAAS

Finding a Needle in a Haystack: Quantitative HERFD-XRF imaging and HERFD-XANES characterization of trace platinum in gold solidi from the Late Roman and Byzantine Empires

Journal:	*Journal of Analytical Atomic Spectrometry*
Manuscript ID	JA-ART-08-2024-000281.R1
Article Type:	Paper
Date Submitted by the Author:	08-Nov-2024
Complete List of Authors:	Van Loon, Lisa; Western University, Anthropology; Western University, Earth Sciences; Western University, Soochow-Western Centre for Synchrotron Radiation Research; LISA CAN Analytical Solutions Inc. Finfrock, Y. Zou; Argonne National Laboratory Advanced Photon Source Meira, Debora; Canadian Light Source Inc Burgess, Richard; University of Ottawa, Department of Classics and Religious Studies Bevan, George; Queen's University, Department of Geography and Planning Banerjee, Neil; Western University, Earth Sciences; Western University, Soochow-Western Centre for Synchrotron Radiation Research

ARTICLE

Finding a Needle in a Haystack: Quantitative HERFD-XRF imaging and HERFD-XANES characterization of trace platinum in gold solidi from the Late Roman and Byzantine Empires

Received 00th January 20xx,
Accepted 00th January 20xx

DOI: 10.1039/x0xx00000x

Lisa L. Van Loon,*[a-d] Y. Zou Finfrock, [e] Debora M. Meira, [f] R. W. Burgess, [g] George Bevan,[h] and Neil R. Banerjee [a, b]

High-Energy Resolution Fluorescence Detection X-Ray Fluorescence (HERFD-XRF) imaging and HERFD X-ray Absorption Near Edge Structure (XANES) spectroscopy are used to quantify and characterize trace platinum (Pt) in gold solidi from the Late Roman and Byzantine Empires. Historically, the elemental analysis of coins has been pivotal in distinguishing authentic artifacts from forgeries, elucidating minting practices, and understanding economic shifts. Notably, a new gold source with high platinum content appeared in the fourth century CE, transforming the Roman economy. Traditional methods struggled to detect platinum due to the overwhelming gold matrix. This study demonstrates the effectiveness of HERFD techniques in resolving this challenge. Three gold solidi, minted between 654 and 659 CE, were analyzed alongside reference gold materials with known Pt concentrations. The HERFD-XRF imaging revealed spatial distributions of platinum, highlighting non-uniformities within the coins. Additionally, HERFD-XANES spectroscopy identified the oxidation states and chemical speciation of platinum. Results demonstrate that platinum in the solidi primarily exists as metallic Pt, with some surface oxidation. The findings align with previous measurements but reveal higher Pt concentrations and significant inhomogeneities. This research confirms the reliability of HERFD methods for quantifying trace elements and provides new insights into the raw material sources and minting techniques of ancient gold coins. The non-destructive nature of this approach allows for extensive analyses, offering valuable data for historical, economic, and archaeological studies. This innovative application of HERFD-XRF imaging and XANES in cultural heritage research underscores the potential for detailed material characterization and conservation, enhancing our understanding of ancient economies and trade patterns.

Introduction

In the field of numismatics, methods for determining the elemental composition of coins have been crucial for distinguishing forgeries from genuine artefacts, characterizing surface plating from bulk materials, identifying the source of raw materials, and understanding minting practices over historical periods.[1–8] Such analyses have provided insights into the economic and geopolitical dynamics of ancient civilizations. One intriguing mystery is a new source of gold that started to appear in the third quarter of the fourth century CE, thought to have originated in Asia Minor or Africa.[9,10] This new gold can easily be distinguished from the existing gold in circulation going back to the early first century CE by its extremely high levels of platinum: whereas earlier gold contained platinum that rarely exceeded 50 ppm, this new gold had levels that were in excess of 2,600 ppm.[11] This new source was massive and prompted the Later Roman Empire's shift from a tri-metallic currency—copper, silver, and gold— to a fundamentally gold-based economy. So great was the quantity of this new gold that by the second quarter of the seventh century, after three hundred years of its being mixed into and absorbed by the massive volume of pre-existing circulating gold, the platinum levels stabilized between 300 and 400 ppm. Given that the fall of the western Roman Empire was fundamentally the result of economic forces, historians want to know exactly when this gold appeared, how it circulated across the empire, and what it can tell us about the economic and political relationships between the eastern and western halves of the empire.

Platinum (Pt) is extremely rare and is typically found as either native platinum or as an alloy with other platinum group elements (PGE).[12] Variations in trace platinum can be used to differentiate between gold sources, providing a fingerprint of the original raw material.[13–18] Platinum is inert with a melting point higher than gold, making it unlikely to be removed during Roman refining processes.[19] Trace platinum and platinum group inclusions have been identified in ancient gold, suggesting their

[a.] Western University, Department of Earth Sciences, London, ON, Canada.
[b.] Western University, Soochow-Western Centre for Synchrotron Radiation Research, London, ON, Canada.
[c.] Western University, Department of Anthropology, London, ON, Canada.
[d.] Lisa Can Analytical Solutions Inc., Saskatoon, SK, Canada.
[e.] Advanced Photon Source, Lemont, IL, USA.
[f.] Canadian Light Source Inc., Saskatoon, SK, Canada.
[g.] University of Ottawa, Department of Classics and Religious Studies, Ottawa, ON, Canada.
[h.] Queen's University, Department of Geography and Planning, Kingston, ON, Canada.

presence can reveal information about the sources and manufacturing techniques of historical gold objects.[19–21]

Synchrotron radiation X-ray fluorescence (SR-XRF) is well-suited for the chemical characterization of metal artefacts because of its non-destructive nature, preserving valuable historical objects.[22–29] The high brilliance of synchrotron sources allows for the detection of trace elements with a high signal-to-noise ratio, and the tunability of the X-ray source optimizes data collection parameters for rapid, sensitive, and non-destructive micro-analysis. However, traditional energy-dispersive detection lacks the resolution needed to distinguish ppm of platinum within a matrix of nearly 99% gold. The energy resolution of an energy-dispersive silicon drift detector (typically around 100 eV) is insufficient for this purpose.[30,31]

A previous study evaluated the use of wavelength-dispersive (WD) detection of SR-XRF signals for the quantitative analysis of trace platinum in Byzantine gold solidi.[32] WD detectors are common in lab-based systems for detecting elements at ppm levels. Unfortunately, their large footprint and short working distance make them challenging to set up at synchrotron beamlines. Aligning a WD detector with a synchrotron beam is complicated, limiting their routine use at synchrotron facilities. Additionally, WD crystal spectrometer setups are designed for specific and limited energy ranges, requiring multiple spectrometers to cover a single beamline's energy range.[33]

A Strip Bent Crytal Analyzer (BCA) allows for effective positioning and use over a typical hard X-ray beamline energy range, making it a practical choice for synchrotron beamlines.[34–36] A BCA achieves high-energy resolution by discriminating the desired Pt fluorescence signal from a large background caused by scatter and fluorescence from the Au matrix.[34,35] High Energy Resolution Fluorescence Detection (HERFD)[37] using a BCA offers better separation of emission lines and rejection of the fluorescence background of neighbouring elements to better image the chemical properties of a sample. The focused beam (using KB mirrors) for high energy resolution and the high flux available at synchrotrons compensate for the much lower signal.[37,38] Several synchrotron beamlines now offer HERFD setups (i.e., at APS, ESRF, DLS), making this approach increasingly accessible.

The combination of a tightly focused beam with the resolution provided by a crystal analyzer allows for energy detection with a smaller bandwidth, leading to spectral sharpening effects. HERFD X-ray Absorption Spectroscopy (XAS) has been used primarily to study catalytic materials,[39–44] and is increasingly being applied in environmental and geological sciences[45–51] and in cultural heritage.[52–55] The higher resolution in HERFD XAS experiments resolves the chemical environment of heavy elements better than conventional XAS,[49,56–58] making it suitable for studying the platinum content in ancient gold artifacts (i.e., inclusions in gold solidi).[59] Combining HERFD with X-ray absorption near-edge structure (XANES) spectroscopy (HERFD-XANES) allows for the high-resolution measurement of the chemical speciation of platinum.[60–62]

Despite the potential of HERFD[63] it has not yet been used for spatial imaging of signals across samples in traditional SR-XRF 2D mapping experiments. Trace platinum's association with native gold suggests it can serve as a tracer for gold sources and manufacturing techniques.[64,65] A microfocusing synchrotron beam combined with HERFD resolution can reveal non-homogeneous distributions of platinum and the presence of inclusions in a HERFD-XRF imaging experiment. By comparing the signal from coins to reference materials with known platinum concentrations, the platinum content in Late Roman and early Byzantine gold solidi can be quantified directly.

Additionally, HERFD-XANES spectroscopy offers greater spectral resolution because the fluorescence signal is associated with a longer lifetime state, providing insights into the oxidation state, adsorbates, and d-band occupancy of platinum.[66] By measuring the Pt HERFD-XANES spectrum and comparing it to known spectra, we can determine whether the platinum in Late Roman and early Byzantine gold solidi is pure metal or an alloy, shedding light on the raw materials used.

In this study, synchrotron-based HERFD spatially resolved XRF imaging (HERFD-XRF) is used to quantify trace platinum in three early Byzantine gold solidi and employ Pt L_3 HERFD-XANES spectroscopic analysis to identify the Pt oxidation state and chemical speciation in those solidi.

Experimental

Three gold solidi minted in Constantinople by the emperors Constans II and Constantine IV between 13 April 654 and 2 June 659 were selected for quantitative Pt analysis using HERFD spatially resolved measurements, Figure 1. The gold fineness of the solidi is 95+ %.[67] The coins were part of previous studies[32,68] and are labelled #2, #3, and #6. The reverses ('tails') of all three coins have been polished to a flat surface. Earlier studies suggest that the platinum levels of solidi of this date should be between 300 and 400 ppm (see above).

Three gold reference materials (CHL A, CHL B, and CHL C) were loaned by the Royal Canadian Mint Assay Department for this study. These standards were developed to assess the purity of gold from 98.4% to 99.99% with known concentrations of nine trace elements. The Pt concentrations are 600, 300, and 12 ppm respectively. All materials were analyzed as received. Prior to measurement, the surfaces were wiped with methanol.

Figure 1. CHL A, and struck obverses of three gold solidi minted in Constantinople by the emperors Constans II and Constantine IV analysed with HERFD-XRF imaging and HERFD-XANES. Each coin is ~ 2 cm dia.

Data Collection

Data collection was performed at the Advanced Photon Source at Beamline 20ID (Argonne National Laboratory, Lemont, IL).[69] The energy was selected using a Si(111) monochromator. The flux at 10 keV is ~10^{13} photons/sec/mm^2 for a 300 µm toroidal-focused beam.

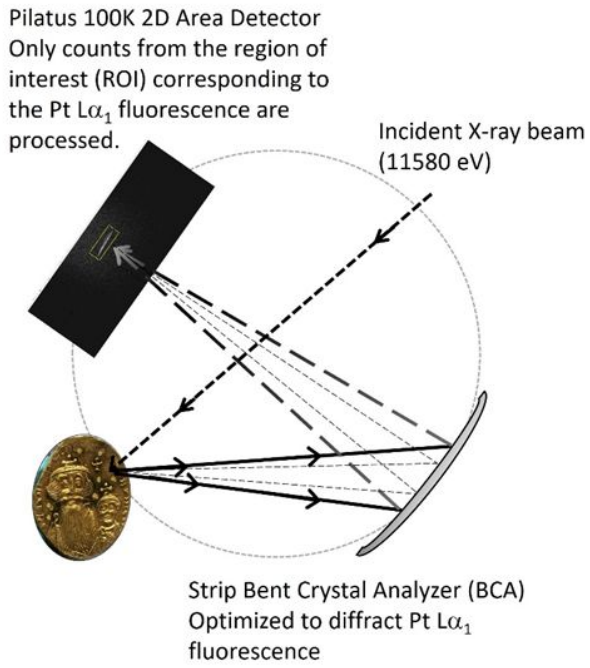

Figure 2. Schematic of the HERFD-XRF imaging and HERFD-XANES spectroscopy setup. The dotted circle outlines the Rowland geometry defining the positions of the sample, BCA, and detector. For the imaging experiments, the incident energy was fixed at 11580 eV. For the HERFD-XANES spectroscopy experiments, the energy was scanned across the Pt L_3-edge from -150 eV – 8k. The signal is measured in the region of interest (ROI) on the 2D area detector.

The geometry of the HERFD setup for the sample, BCA, and detector is defined by a Rowland circle. The BCA used has a 0.5 m radius optimized to diffract Pt $L_{\alpha1}$ fluorescence. The diffracted signal is directed to a Pilatus 100K 2D area detector (Dectris Ltd., Switzerland) that counts the spatially resolved photons from the sample and diffracted by the crystal, Figure 2.[60] The spatially separated region of interest (ROI) corresponding to the Pt signal was identified and only counts from that ROI were processed.

HERFD-XRF Imaging

HERFD-XRF Pt distribution maps (6000 µm x 3000 µm or 10000 µm x 10000 µm) were created by rastering in the x and y directions in 300 µm steps (21 x 11 or 34 x 34 pixels) with a 500 msec dwell time per point. The beam size was 300 µm. An incident energy of 11580 eV (Pt L_3 = 11564 eV) was selected.[32] For the three solidi, Pt maps were collected on both the polished reverses and the struck obverses.

HERFD XANES Spectroscopy

The Pt L_3 XANES region was scanned from -150 eV to 8k relative to the Pt L_3-edge with an integration time of 1 sec/point. For the 3 solidi, XANES spectra were collected on both the polished reverses and the struck obverses. The Pt metal transmission XANES and HERFD-XANES spectra were collected using a Pt metal foil (Exafs Materials, California).

Data Processing

Maps of Pt distribution were created in OriginPro 2021.[70] The XANES spectra were analysed using the X-ray absorption spectroscopy data processing software, Athena.[71] Sample spectra were calibrated at the Pt L_3-edge to 11564 eV using the second derivative spectrum of the Pt foil. The spectra were background corrected by subtracting a straight line fit to the pre-edge from the entire spectrum. The spectra were normalized to a per-atom basis by using a straight line fit to the post-edge region of the XANES spectra. All additional analyses were performed using Origin 2021.

Results and discussion

Platinum L_3-edge HERFD-XANES spectra of gold reference materials and Byzantine gold solidi

The Pt L_3-edge HERFD-XANES spectra were collected for a platinum metal foil, the three reference materials (CHL A, B, and C) as well as the three solidi on both the polished reverses ('tails') and struck obverses ('heads'). The transmission XANES and HERFD-XANES spectra of the Pt foil are shown in Figure 3. As has been previously observed[60] the transmission XANES spectrum has a longer tail on the low energy side. The white line of the HERFD-XANES spectrum is much more intense.[72] The peaks are sharper and more resolved than in the transmission XANES spectrum.

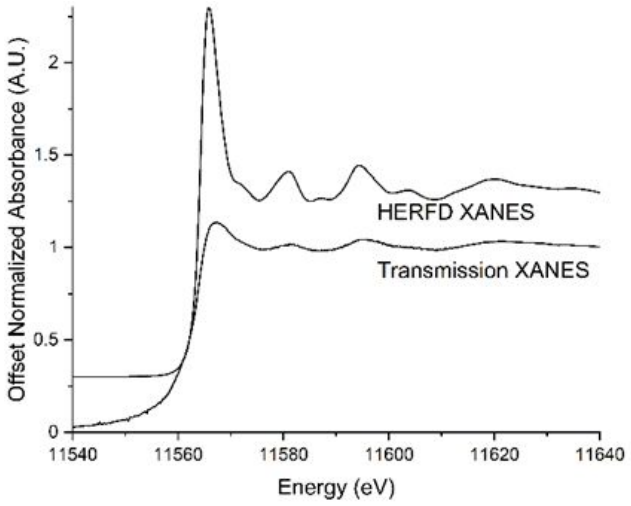

Figure 3. Platinum L_3-edge HERFD-XANES (top) and transmission (bottom) spectra collected for a Pt metal foil. The spectra are offset for clear viewing.

The Pt L_3-edge HERFD-XANES spectra collected for CHL A, B, and C are shown in Figure 4. With decreasing concentrations, the HERFD-XANES spectra become noisier and the CHL C spectrum is the noisiest as it is the reference material with the lowest Pt concentration (12 ppm). The spectra agree with that of the Pt^0 foil. However, the first peaks in the CHL reference spectra are wider than that of Pt^0. This may be due to minor surface oxidation. The spectral features at ~11580 eV and ~11593 eV are resolved for CHL A and CHL B and match those of Pt^0.

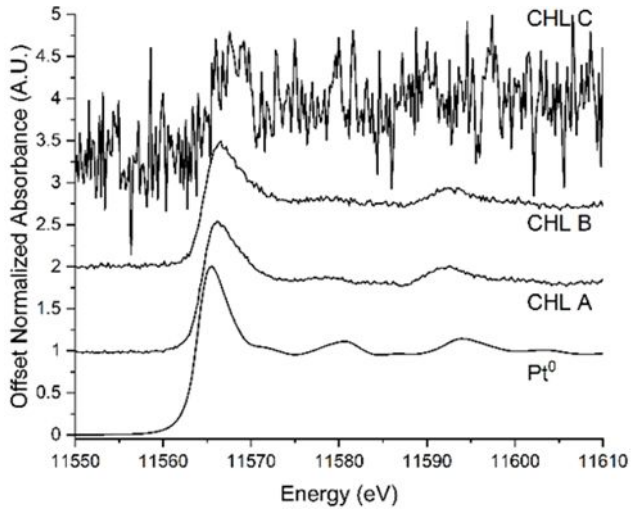

Figure 4. Platinum L_3-edge HERFD-XANES spectra of a Pt foil (bottom), CHL A (600 ppm Pt), CHL B (300 ppm Pt), and CHL C (12 ppm Pt). As the Pt concentration decreases, the HERFD-XANES signal becomes noisier. The spectra are offset for clear viewing.

The Pt L_3-edge HERFD-XANES spectra collected on the polished reverses and struck obverses of the coins are shown in Figure 5. The spectra from both the reverses (polished) and obverses are the same. The noise level of the spectra collected on the polished sides of the coins is like that of the spectrum collected for CHL B, which has a similar Pt concentration. The spectra collected for Coin 6 are shifted to higher energy relative to those of Coins 2 and 3, and CHL B.

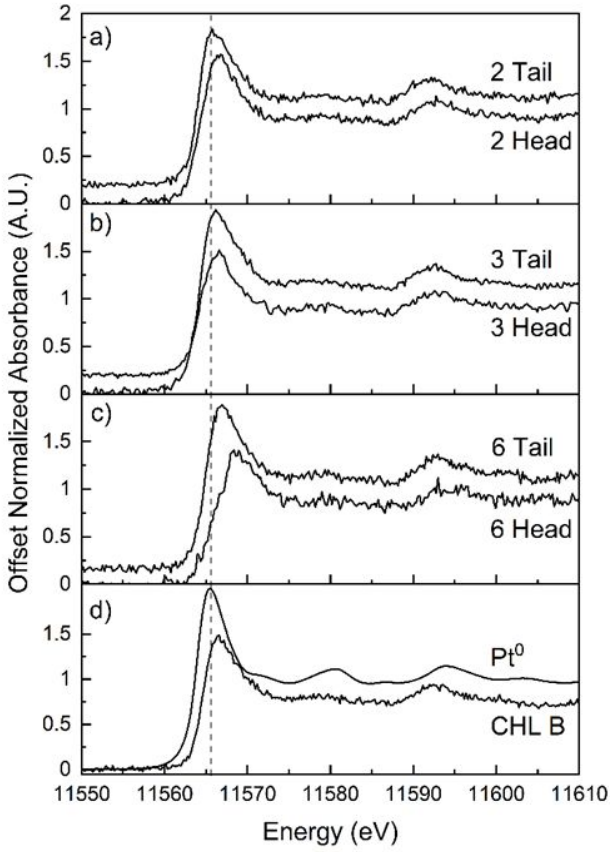

Figure 5. Platinum L_3-edge HERFD-XANES spectra of a) Coin 2, b) Coin 3, c) Coin 6, and d) Pt^0 and CHL B. A spectrum was collected on both the reverses ("Tail") and the obverses ("Head") of each coin. The dotted line is a guide for the eye to the first peak. The peak positions of Coins 2 and 3 agree with that for CHL B. The first peak position for Coin 6 is shifted to higher energy.

HERFD mapping of platinum in RCM gold reference materials

The reference materials CHL A, CHL B, and CHL C were mapped using HERFD-XRF imaging to determine the spatial distribution of Pt within each of the three (3) reference materials over a (6000 µm x 3000 µm; 231 pixels) area. The variation in the spatial distribution of Pt within each reference material is shown in Figure 6. The reference materials are well-mixed with a low standard deviation, and this is reflected in the maps. For comparison, the HERFD-XRF Pt maps for the three reference materials are shown on a single intensity scale to reflect the difference in concentrations between CHL A (12 ppm Pt), B (300 ppm Pt) and C (600 ppm Pt). In these maps, little variation in colour – which corresponds to variation in Pt concentration – is observed, again confirming that the reference materials are well-mixed.

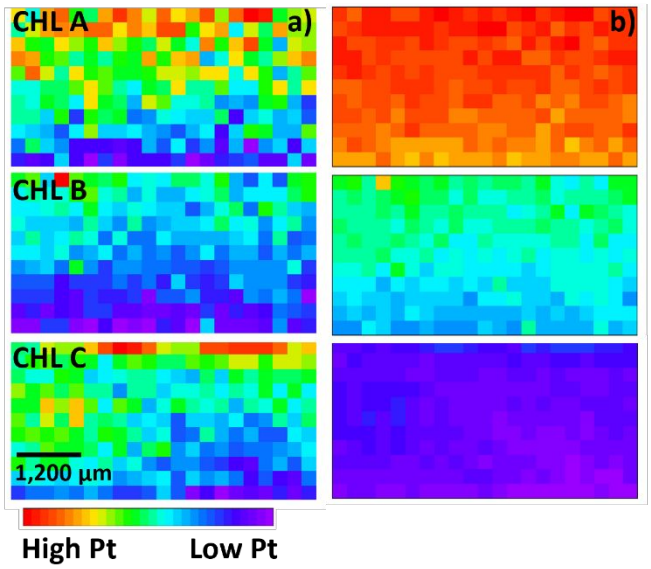

Figure 6. HERFD-XRF images of Pt in the three (3) CHL Au reference materials. Each map is (6000 µm x 3000 µm). The maps were collected using a 300 µm spot size and step size. a) The relative Pt concentrations for each reference material are represented using a colour scale from red (high Pt) to purple (low Pt). The variation in colour reflects the standard deviations reported in Table 1. The colour scale reflects the relative Pt concentrations within each sample. b) The relative platinum concentrations between the three reference materials are represented using a colour scale from red (high Pt) to purple (low Pt). The variation in colour reflects the differences in the concentrations of Pt in the three reference materials: CHL A = 600 ppm, CHL B= 300 ppm, and CHL C = 12 ppm.

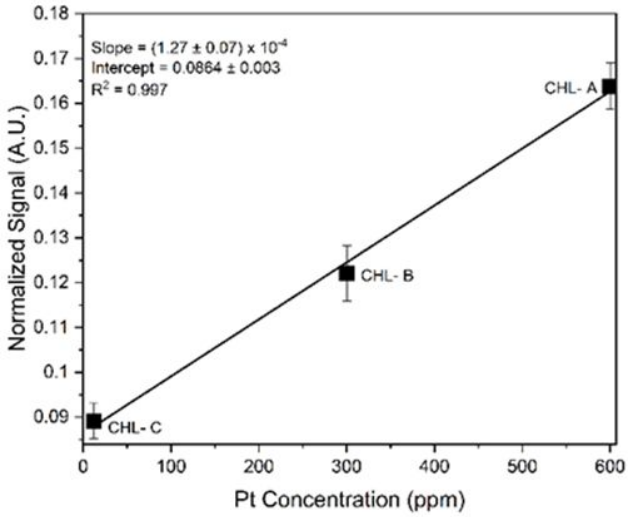

Figure 7. Line of best fit of the averaged intensity of the HERFD-XRF signal measured as a function of Pt concentration for the three CHL reference materials: CHL A = 600 ppm, CHL B= 300 ppm, and CHL C = 12 ppm. Both the reference materials and the samples can be assumed to be infinitely thick (greater than the minimum thickness needed to absorb all the X-rays of the primary X-ray beam). As a result, the determined intercept and slope are used to calculate Pt concentrations in the three coins.

The average HERFD-XRF intensity for each map is reported in Table 1. The reference materials are well mixed with standard deviations of 3-4%. A calibration curve was prepared using the average intensity, Figure 7, and a least-squares fitting analysis was done to determine the trace Pt concentrations in a gold matrix. The calibration curve shows a linear response over the measured Pt concentration range, $R^2 = 0.997$, indicating that the HERFD-XRF analysis is suitable for the quantitative determination of trace Pt concentrations in a gold matrix.

Table 1. Average measured HERFD-XRF Pt L_3 intensity for each mapped region (6000 µm x 3000 µm) collected for the three RCM gold reference materials CHL A, B, and C.

	Pt concentration (ppm)	Average measured Pt-L_3 Signal (x 10^3, A.U.)[a]
CHL A	600	164 ± 5
CHL B	300 ± 9[b]	122 ± 6
CHL C	12	89 ± 4

a. Errors reported are the standard deviations of each map. Errors associated with counting statistics and beamline setup are well below the reported errors.

b. The error is reported in the assay report for CHL B and so is included here.

HERFD quantification of platinum concentrations in Byzantine gold solidi

Intensity maps of the HERFD-XRF signal were collected on both the polished reverse and the struck obverse of each coin, Figures 8 and 9 respectively, with the same sample to detector distance. The maps of both the reverses and obverses of all coins show variation in the spatial distribution of Pt within each coin. Visual comparison of the scaled maps (right columns, Figures 8 and 9) with those of the CHL reference materials (Figure 6) shows that the Pt concentrations in the coins are most like that of CHL B (300 ppm Pt). The calculated Pt concentrations for each mapped region are found in Table 2. The standard deviations indicate that there is greater variation in the Pt distribution in the coins, which is represented visually by the variation in colour in the maps.

For the HERFD-XRF maps collected on the reverses ('tails') of the coins there is a 22 – 27% variation in Pt concentration within each coin. For the maps collected on the obverses ('heads') there is a 29 – 35% variation in Pt concentration within each coin. The maps collected on the struck sides of Coins 2 and 3 both reveal Pt hotspots with maximum Pt values of 2737 ppm and 1175 ppm respectively.

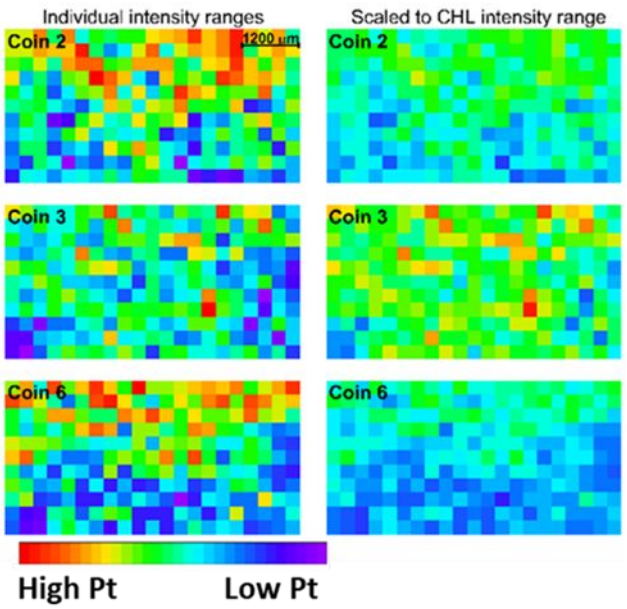

Figure 8. HERFD-XRF images of Pt collected on the reverses of Coins 2, 3, and 6. The left column are maps with individual intensity scalings to show the variation in Pt distribution within each coin. The relative Pt concentrations are represented using a colour scale from red (high Pt) to purple (low Pt). The variation in colour reflects the standard deviations reported in Table 2. The right column shows the same maps scaled to the CHL intensity range in Figure 6 b) so the coin maps can be compared to those of the RCM reference materials. The maps of the coins are most similar to those for RCM reference material CHL B (Pt = 300 ppm). Differences in the range of colour reflects that Coin 2 has the highest measured Pt concentration and Coin 6 has the lowest.

The average Pt concentrations determined for the reverses agree with previously measured values. Coin 3 has the highest Pt concentration. In this study, Coin 2 has a higher Pt concentration than Coin 6, different from the SR-WD-XRF analysis, but in agreement with the SA-ICP-OES measurements.[32] For the maps collected on the obverses, the measured concentrations in this HERFD-XRF study are higher than previously measured using SR-WD-XRF[32] and Coin 2 has the highest average Pt concentration.

The maps collected on the reverse of Coin 3 shows the most variation in the Pt distribution as well as Pt hotspots. The maps collected on the obverse sides of Coins 2 and 3 show variation in the Pt distribution and hotspots. This spatial variation is only revealed using a spatial mapping analysis. The variation indicates that Pt is not distributed uniformly in the gold used in manufacturing these coins. The heat used was likely sufficient to melt and pour the gold but the temperature was not high enough to melt and mix in the Pt homogeneously.

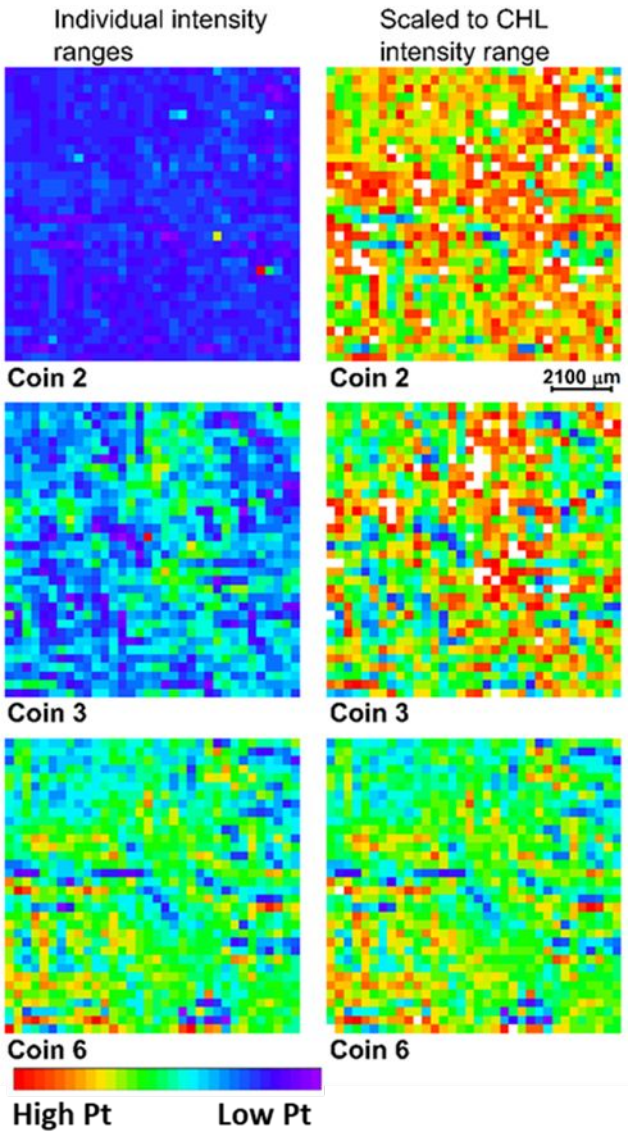

Figure 9. HERFD-XRF images of Pt collected on the obverses of Coins 2, 3, and 6. The left column are maps with individual intensity scalings to show the variation in Pt distribution within each coin. The relative Pt concentrations are represented using a colour scale from red (high Pt) to purple (low Pt). The variation in colour reflects the standard deviations reported in Table 2. The right column shows the same maps scaled to the CHL intensity range used in Figure 6 b) so the coin maps can be compared to those of the RCM reference materials. The maps of the coins are most similar to those for RCM reference material CHL B (Pt = 300 ppm). Differences in the range of colour reflects that Coin 2 has the highest measured Pt concentration and Coin 6 has the lowest.

Table 2. Calculated Pt concentrations for Coins 2, 3, and 6 determined for both the reverses (polished) and obverses (struck).

	Reverse Pt concentration (ppm)[a] (N = 341)	Obverse Pt concentration (ppm)[a] (N = 1156)
Coin #2	302 ± 68	508 ± 147
Coin #3	376 ± 86	438 ± 148
Coin #6	243 ± 65	373 ± 107

a. Errors reported are the standard deviations of each map. Errors associated with counting statistics and beamline setup are well below the reported errors.

Conclusions

This study demonstrates the efficacy of High-Energy Resolution Fluorescence Detection (HERFD) imaging for the spatially resolved and quantitative analysis of trace platinum (Pt) in an early Byzantine solidus matrix. Utilizing HERFD imaging spatial mapping, low concentrations of Pt within gold solidi were quantified. The high flux from a synchrotron source enabled the detection of trace Pt with remarkable precision. The high-resolution capabilities of the HERFD imaging reveals the variable spatial distribution of Pt within a single coin.

HERFD XANES spectroscopic analysis indicates that Pt within these coins predominantly exists as Pt metal, with some Pt oxide likely present at the coin surfaces. This compositional information can provide insights into the sources of the gold used during the Late Roman and early Byzantine eras. The comparative analysis with three gold reference materials confirmed the reliability of HERFD imaging for quantifying Pt concentrations, aligning with results from other established techniques such as SR-WD-XRF and SA-ICP-OES.[32,68] This study highlights the unique advantage of HERFD-XRF imaging in detecting inhomogeneities in Pt distribution, which traditional bulk measurement techniques may overlook.

The application of HERFD-XRF imaging and XANES in cultural heritage studies, as illustrated by this research, represents a novel approach to investigating historical artifacts. The ability to perform rapid, non-destructive quantitative analyses on many coins opens up possibilities for extensive statistical studies and a deeper understanding of historical minting practices, ancient economies and trade patterns, and raw material sources.

The application of HERFD-XRF imaging and XANES spectroscopy extends to several fields:

1. Materials Characterization: This study is one of the first examples of HERFD-XRF imaging to achieve high sensitivity and spatial resolution in trace element analysis. The ability to perform element mapping in combination with high-resolution XANES makes synchrotron techniques the gold standard for detailed material characterization.

2. Historical Insights: The precise quantification and spatial mapping of trace Pt in Late Roman and early Byzantine coins provides new, non-destructive approaches to gain insights into the sources of gold used between the middle of the fourth and middle of the seventh centuries. Through the analysis of a statistically significant number of coins, variations in minting practices, trade patterns, imperial tax collection, and regional differences in raw material sources could be determined. These scientific insights could help historians and archaeologists trace the origin of raw materials and understand the economic and geopolitical factors that influenced coin production, distribution, and debasement, and, hence, ancient economies.

Future work could leverage the sensitivity of Pt L_3 HERFD-XANES to further explore the chemical state and alloy compositions of Pt inclusions. Such studies could offer additional insights into the metallurgical practices and provenance of materials used in the Late Roman and early Byzantine Empires.

3. Conservation: The combination of HERFD-XRF imaging and XANES could inform conservation efforts. The non-destructive nature ensures that priceless artifacts can be studied without damage, preserving them for future generations. The detailed compositional data obtained can guide the development of effective preservation techniques.

Author contributions

The manuscript was written through contributions of all authors. All authors have given approval to the final version of the manuscript.

Conflicts of interest

There are no conflicts to declare.

Data availability

The authors confirm that the data supporting the findings of this study are available within the article.

Acknowledgements

The authors gratefully thank the Royal Canadian Mint for the loan of reference materials. This research used resources of the Advanced Photon Source, an Office of Science User Facility operated for the U.S. Department of Energy (DOE) Office of Science by Argonne National Laboratory, and was supported by the U.S. DOE under Contract No. DE-AC02-06CH11357, and the Canadian Light Source and its funding partners.

This research was supported by grants from the Natural Sciences and Engineering Research Council (NSERC) of Canada to N.R. Banerjee.

References

1 M. O. Pereira, V. De, S. Felix, P. De, J. M. Aranha, P. C. S. Heringer and R. P. Freitas, in *INAC2017: International Nuclear Atlantic Conference*, 2017, p. 6.

2 M. Guerra, in *Chemical Analysis in Cultural Heritage*, eds. L. Sabatini and I. van der Werf, Walter de Gruyter, 2020, pp. 307–330.

3 M. F. Guerra and T. Calligaro, *J. Archaeol. Sci.*, 2004, **31**, 1199–1208.

4 M. F. Guerra and T. Calligaro, *Meas. Sci. Technol.*, 2003, **14**,

1527–1537.

5 M. F. Guerra, C. O. Sarthre, A. Gondonneau and J. N. Barrandon, *J. Archaeol. Sci.*, 1999, **26**, 1101–1110.

6 M. F. Guerra, in *Cultural Heritage Conservation and Environmental Impact Assessment by Non-Destructive Testing and Micro-Analysis*, eds. R. Van Grieken and K. Janssens, CRC Press, 2004, pp. 231–252.

7 A. Oddy, *Gold Bull.*, 1988, **2**, 29–36.

8 M. F. Guerra, in *Radiation in Art and Archeometry*, eds. D. C. Creagh and D. A. Bradley, Elsevier Science B.V., 2000, pp. 378–416.

9 S. Vryonis Jr., *Speculum A J. Mediaev. Stud.*, 1962, **37**, 1–17.

10 C. Meyer, *Bir Umm Fawakhir Survey Project 1993: A Byzantine Gold-mining Town in Egypt, Vol. 1*, 2000.

11 C. Morrisson, C. Brenot, J.-P. Callu, J.-N. Barrandon, J. Poirier and R. Halleux, *L'or monnayé I: purification et altérations de Rome à Byzance (Cahiers Ernest-Babelon II)*, Editions du Centre national de la recherche scientifique, Paris, 1985.

12 M. L. Zientek, P. J. Loferski, H. L. Parks, R. F. Schulte and R. R. Seal II, *Platinum-group elements*, Reston, VA, 2017.

13 H. Liu, G. Beaudoin, S. Makvandi, S. E. Jackson and X. Huang, *Ore Geol. Rev.*, 2021, **131**, 104061.

14 R. K. W. Merkle, R. D. Dixon and A. Kijko, in *Applied Mineralogy: Developments in Science and Technology*, ed. M. Pecchio, International Council for Applied Mineralogy, Sao Paulo, 2004, pp. 901–904.

15 D. Lesigyarski, B. Zlateva, V. Lyubomirova, T. Stoyanov and I. Kuleff, *ArcheoSciences*, 2015, 149–156.

16 M. F. Guerra, T. Calligaro, M. Radtke, I. Reiche and H. Riesemeier, *Nucl. Instruments Methods Phys. Res. Sect. B Beam Interact. with Mater. Atoms*, 2005, **240**, 505–511.

17 S. Schlosser, R. Kovacs, E. Pernicka, D. Günther and M. Tellenbach, in *New Technologies for Archaeology. Natural Science for Archaeology*, eds. M. Reindel and G. A. Wagner, Springer, Heidelberg, 2009, pp. 409–436.

18 S. Schlosser, A. Reinecke, R. Schwab, E. Pernicka, S. Sonetra and V. Laychour, *J. Archaeol. Sci.*, 2012, **39**, 2877–2887.

19 L. Dussubieux and L. Van Zelst, *Appl. Phys. A Mater. Sci. Process.*, 2004, **79**, 353–356.

20 M. Radtke, G. Buzanich, A. Guilherme, U. Reinholz, H. Riesemeier, O. Scharf, P. Scholz and M. F. Guerra, *Microchem. J.*, 2016, **125**, 56–61.

21 M. Jansen, S. Aulbach, A. Hauptmann, H. E. Höfer, S. Klein, M. Krüger and R. L. Zettler, *J. Archaeol. Sci.*, 2016, **68**, 12–23.

22 L. Bertrand, M. Cotte, M. Stampanoni, M. Thoury, F. Marone and S. Schöder, *Phys. Rep.*, 2012, **519**, 51–96.

23 L. Bertrand, L. Robinet, M. Thoury, K. Janssens, S. X. Cohen and S. Schöder, *Appl. Phys. A Mater. Sci. Process.*, 2012, **106**, 377–396.

24 M. F. Guerra, M. Radtke, I. Reiche, H. Riesemeier and E. Strub, *Nucl. Instruments Methods Phys. Res. Sect. B Beam Interact. with Mater. Atoms*, 2008, **266**, 2334–2338.

25 M. Rodrigues, M. Schreiner, M. Melcher, M. Guerra, J. Salomon, M. Radtke, M. Alram and N. Schindel, *X-Ray Spectrom.*, 2012, **41**, 416–424.

26 M. Rodrigues, F. Cappa, M. Schreiner, P. Ferloni, M. Radtke, U. Reinholz, B. Woytek and M. Alram, *J. Anal. At. Spectrom.*, 2011, **26**, 984–991.

27 B. Constantinescu, A. Vasilescu, D. Stan, M. Radtke, U. Reinholz, G. Buzanich, D. Ceccato and E. Oberländer-Târnoveanu, *J. Anal. At. Spectrom.*, 2012, **27**, 2076–2081.

28 A. Vasilescu, B. Constantinescu and R. Bugoi, *Rom. Reports Phys.*, 2011, **56**, 266–272.

29 M. L. Young, *Reports Prog. Phys.*, 2012, **75**, 036504.

30 K. Thompson, *Micros. Today*, 2013, **21**, 30–34.

31 Silicon Drift Detectors (SDD), https://www.hitachi-hightech.com/hhs-us/product_detail/?pn=ana-vortex-me4, (accessed 24 September 2021).

32 L. L. Van Loon, N. R. Banerjee, M. W. Hinds, R. Gordon, G. Bevan and R. W. Burgess, *J. Anal. At. Spectrom.*, 2018, **33**, 1763–1769.

33 Oxford Instruments Analytical, *Wavelength Dispersive X-ray Microanalysis Explained*, 2002.

34 C. Karanfil, G. Bunker, M. Newville, C. U. Segre and D. Chapman, *J. Synchrotron Radiat.*, 2012, **19**, 375–380.

35 G. Bunker, *Introduction to XAFS A Practical Guide to X-ray Absorption Fine Structure Spectroscopy*, Cambridge University Press, Cambridge, First Edit., 2010.

36 Z. Zhong, D. Chapman, B. Bunker, G. Bunker, R. Fischetti and C. Segre, *J. Synchrotron Radiat.*, 1999, **6**, 212–214.

37 P. Glatzel, F. M. F. De Groot, O. Manoilova, D. Grandjean, B. M. Weckhuysen, U. Bergmann and R. Barrea, *Phys. Rev. B - Condens. Matter Mater. Phys.*, 2005, **72**, 1–7.

38 U. Bergmann, L. Bertrand, N. P. Edwards, P. L. Manning and R. A. Wogelius, in *Synchrotron Light Sources and Free-Electron Lasers*, 2020, pp. 2393–2455.

39 M. Bauer, *Phys. Chem. Chem. Phys.*, 2014, **16**, 13827–13837.

40 J. Wang, C. S. Hsu, T. S. Wu, T. S. Chan, N. T. Suen, J. F. Lee and H. M. Chen, *Nat. Commun.*, 2023, **14**, 6576.

41 B. C. Vicente, R. C. Nelson, J. Singh, S. L. Scott and J. A. Van Bokhoven, *Catal. Today*, 2011, **160**, 137–143.

42 J. Singh, R. C. Nelson, B. C. Vicente, S. L. Scott and J. A. van Bokhoven, *Phys. Chem. Chem. Phys.*, 2010, **12**, 5668–5677.

43 S. Kobayashi, W. Cao, Y. Gao, T. Uchiyama, H. Imai, Y. Sakurai, Y. Tsuji and Y. Uchimoto, *ECS Meet. Abstr.*, 2022, **MA2022-02**, 1565.

44 S. Kaya, D. Friebel, H. Ogasawara, T. Anniyev and A. Nilsson, *J. Electron Spectros. Relat. Phenomena*, 2013, **190**, 113–124.

45 S. M. Hayes, R. J. McAleer, N. M. Piatak, S. J. O. White and R. R. Seal, *Front. Earth Sci.*, 2023, **11**, 939700.

46 E. M. Saurette, Y. Z. Frinfrock, B. Verbuyst, D. W. Blowes, J. M. Mcbeth, C. J. Ptacek and D. Bhattacharyya, *J. Synchrotron Radiat.*, 2022, **29**, 1198–1208.

47 J. C. Swarbrick, U. Skyllberg, T. Karlsson and P. Glatzel, *Inorg. Chem.*, 2009, **48**, 10748–10756.

48 O. Proux, E. Lahera, W. Del Net, I. Kieffer, M. Rovezzi, D. Testemale, M. Irar, S. Thomas, A. Aguilar-Tapia, E. F. Bazarkina, A. Prat, M. Tella, M. Auffan, J. Rose and J.-L. Hazemann, *J. Environ. Qual.*, 2017, **46**, 1146–1157.

49 K. O. Kvashnina, S. M. Butorin, P. Martin and P. Glatzel,

Phys. Rev. Lett., 2013, **111**, 1–5.

50 G. S. Pokrovski, E. Desmaele, C. Laskar, E. F. Bazarkina, D. Testemale, J. L. Hazemann, R. Vuilleumier, A. P. Seitsonen, G. Ferlat and A. M. Saitta, *Am. Mineral.*, 2022, **107**, 369–376.

51 G. S. Pokrovski, C. Escoda, M. Blanchard, D. Testemale, J. L. Hazemann, S. Gouy, M. A. Kokh, M. C. Boiron, F. De Parseval, T. Aigouy, L. Menjot, P. De Parseval, O. Proux, M. Rovezzi, D. Béziat, S. Salvi, K. Kouzmanov, T. Bartsch, R. Pöttgen and T. Doert, *Geochemical Perspect. Lett.*, 2021, **17**, 39–44.

52 L. Monico, M. Cotte, F. Vanmeert, L. Amidani, K. Janssens, G. Nuyts, J. Garrevoet, G. Falkenberg, P. Glatzel, A. Romani and C. Miliani, *Anal. Chem.*, 2020, **92**, 14164–14173.

53 C. Costantino, L. Monico, F. Rosi, R. Vivani, A. Romani, L. C. Colocho Hurtarte, E. Villalobos-Portillo, C. J. Sahle, T. Huthwelker, C. Dejoie, M. Burghammer and M. Cotte, *Appl. Spectrosc.*, 2024, 1–14.

54 M. Cotte, K. Dollman, V. Fernandez, V. Gonzalez, F. Vanmeert, L. Monico, C. Dejoie, M. Burghammer, L. Huder, S. Fisher, W. de Nolf, I. Fazlic, H. Castillo-Michel, M. Salomé, M. Ghirardello, D. Comelli, O. Mathon and P. Tafforeau, *Synchrotron Radiat. News*, 2022, **35**, 3–9.

55 G. Calas, L. Galoisy, M. O. J. Y. Hunault, P. Rautiyal, K. Skerratt-Love, J. C. Rigby and P. A. Bingham, *J. Cult. Herit.*, 2023, **59**, 93–101.

56 P. Glatzel, Introduction to XAS/XES, http://pieter-glatzel.de/XASXES.html, (accessed 27 January 2024).

57 H. Hu, J. Zhao, L. Wang, L. Shang, L. Cui, Y. Gao, B. Li and Y. F. Li, *TrAC - Trends Anal. Chem.*, 2020, **122**, 115721.

58 J. M. Ablett, S. R. Shieh, V. Balédent, J. C. Woicik, E. Cockayne and E. L. Shirley, *Phys. Rev. B*, 2021, **104**, 1–8.

59 N. P. Edwards, J. R. Bargar, D. Van Campen, A. Van Veelen, D. Sokaras, U. Bergmann and S. M. Webb, *Rev. Sci. Instrum.*, 2022, **93**, 083101.

60 J. Chen, Y. Z. Finfrock, Z. Wang and T. K. Sham, *J. Phys. Chem. C*, 2021, **125**, 2327–2333.

61 D. Friebel, D. J. Miller, C. P. O'Grady, T. Anniyev, J. Bargar, U. Bergmann, H. Ogasawara, K. T. Wikfeldt, L. G. M. Pettersson and A. Nilsson, *Phys. Chem. Chem. Phys.*, 2011, **13**, 262–266.

62 C. Laskar, E. F. Bazarkina, M. A. Kokh, J. L. Hazemann, S. Foulon, O. Leynaud, E. Desmaele and G. S. Pokrovski, *Minerals*, 2022, **12**, 1602.

63 U. Bergmann, M. Ivanovic, P. Glatzel and S. P. Cramer, *IEEE Trans. Nucl. Sci.*, 2003, **50**, 140–145.

64 A. Adriaens, *Spectrochim. Acta - Part B At. Spectrosc.*, 2005, **60**, 1503–1516.

65 R. S. Jones and M. Fleischer, *Gold in minerals and the composition of native gold*, 1969.

66 J. Timoshenko and B. Roldan Cuenya, *Chem. Rev.*, 2021, **121**, 882–961.

67 F. Delamare and P. Montmitonnet, *J. Mech. Work. Technol.*, 1984, **10**, 253–271.

68 M. W. Hinds, G. Bevan and R. W. Burgess, *J. Anal. At. Spectrom.*, 2014, **29**, 1799–1805.

69 S. Heald, E. Stern, D. Brewe, R. Gordon, D. Crozier, D. Jiang and J. Cross, *J. Synchrotron Radiat.*, 2001, **8**, 342–344.

70 *OriginPro, Version 2021*, OriginLab Corporation, Northampton, MA, USA.

71 B. Ravel and M. Newville, *J. Synchrotron Radiat.*, 2005, **12**, 537–541.

72 S. Hayama, R. Boada, J. Chaboy, A. Birt, G. Duller, L. Cahill, A. Freeman, M. Amboage, L. Keenan and S. Diaz-Moreno, *J. Phys. Condens. Matter*, 2021, **33**, 284008.

Data availability

The authors confirm that the data supporting the findings of this study are available within the article.